Journal of Translational Medicine

RESEARCH

Open Access

Single-cell and spatial transcriptomic analysis reveals PAX5's role and regulatory mechanisms in gastric adenocarcinoma lymph node metastasis

Shi Chen[1†], Feng Wang[1†], LiXing Wang[1†], Yun Gong[1], YiJun Li[1], QingWen Xu[1], LinXing He[1], YuXing Qi[1], ShuMin Li[1], Hang Xiong[1], Chen Liao[1*] and Feng Sun[1*]

Abstract

Background Lymph node metastasis (LMN) is a key factor in the poor clinical prognosis of patients with gastric adenocarcinoma (GAC), but the underlying cellular regulatory networks and molecular mechanisms are not fully understood.

Methods A combined approach of single-cell RNA sequencing (scRNA-seq) and spatial transcriptomics (ST) was employed to characterize the cellular landscape of the GAC lymph node metastasis microenvironment. Critical regulatory genes were screened. Their roles and underlying molecular mechanisms were then confirmed via in vitro and in vivo functional assays.

Results Eight core cell types were identified by scRNA-seq, with proliferative cell clusters further subdivided into six proliferative subpopulations, including proliferative B cells. ST revealed the presence of tertiary lymphoid structures (TLS) formed by T/B cell aggregates within tumor regions of each lesion. Proliferative B cells exhibited dynamic functional transitions. During the primary lesion (PL) stage, their function was primarily associated with regulating apoptosis. In the metastatic primary lesion (MPL) stage, this shifted to participating in T cell/NK cell activation. In the metastatic lymph node (MLN) stage, an immune evasion network was constructed through pathways such as mediating Th2-biased immune responses and uncontrolled somatic diversification of immune receptors. Lasso regression combined with a random forest model confirmed PAX5 as a highly significant regulatory gene for predicting the functional characteristics of proliferative B cells. Its expression levels progressively increased with tumor metastasis (MLN > MPL > PL, $p < 0.0001$). In vivo and in vitro studies confirmed PAX5's pro-tumorigenic role, promoting proliferation by activating PI3K/AKT1 signaling and upregulating VEGF-C.

†Shi Chen, Feng Wang and LiXing Wang contributed equally to this work.

*Correspondence:
Chen Liao
13987166877@163.com
Feng Sun
SunFeng1971@163.com

Full list of author information is available at the end of the article

Conclusions The systematic characterization of proliferative B cell functional dynamics, from anti-tumor immunity to immune evasion, was achieved. PAX5 was confirmed as a critical regulator of proliferative B cell function, mediating tumor progression through the VEGF-C/PI3K/AKT1 pathway.

Keywords Gastric adenocarcinoma, Lymph node metastasis, PAX5, Single-cell RNA sequencing, Spatial transcriptomics, PI3K/AKT1

Introduction

Gastric adenocarcinoma (GAC), as the most common histological subtype of gastric malignancies (accounting for approximately 95%), has become one of the most lethal cancers globally due to its strong invasiveness, proneness to treatment resistance, and high metastatic potential [1, 2]. Statistics show that GAC accounts for 5.6% of newly diagnosed cancer cases and 7.7% of cancer deaths worldwide [3]. Lymph node metastasis (LNM) represents a critical juncture in the progression of GAC and is closely associated with patient prognosis. Once it occurs, the survival rate of patients decreases significantly, and the difficulty of treatment surges dramatically [4]. Therefore, an in-depth exploration of the cellular and molecular mechanisms underlying the progression from the early onset to metastasis of GAC is of paramount importance for the development of effective treatment strategies.

The tumor microenvironment (TME) plays a pivotal role in tumorigenesis, progression, and metastasis, comprising a diverse array of cell types including tumor, immune, stromal, and endothelial cells. Their dynamic interactions form a complex network that regulates tumor biology [5]. Tumor cells can activate specific signaling pathways to enhance their metastatic potential, concurrently influencing the LNM [6]. For instance, molecular markers such as LYVE-1, Prox1, and podoplanin, expressed by lymphatic endothelial cells, undergo alterations within the TME, which facilitates the initial lymphatic uptake of tumor cells and their subsequent transport to lymph nodes [7]. Moreover, tumor cells may remodel the structure and permeability of lymph node vasculature to acquire increased nutrients and oxygen to support their growth. Specifically, the VEGF-C-mediated signaling pathway can promote lymphangiogenesis in lymph nodes, thereby augmenting opportunities for tumor cell metastasis to these sites [8, 9].

The emergence of single-cell RNA sequencing (scRNA-seq) technology has enabled the assessment of thousands of cells at single-cell resolution, facilitating the elucidation of subtle differences in tumor cell heterogeneity and the complexities of TME [10]. Utilizing this approach, studies have revealed that the GAC microenvironment comprises various stromal cell types, including fibroblasts, neurons, endothelial cells, and immune cells [11]. Concurrently, spatial transcriptomics (ST) technology provides comprehensive spatial gene expression maps at the tissue section level [12]. When integrated with scRNA-seq, ST facilitates the characterization of cellular alterations within tissue architecture and helps to elucidate the functional relationships between distinct cell clusters and histological structures [13].

Based on these observations, this study aims to integrate scRNA-seq and ST to comprehensively analyze the cellular landscape of the GAC lymph node metastasis microenvironment and uncover potential underlying mechanisms driving tumor progression. Systematically analyzing surgically resected samples from GAC patients, we anticipate identifying cell types and key genes closely associated with LNM, thereby providing novel insights and biomarkers for precision treatment and prognosis assessment of GAC. Furthermore, this study will utilize cellular and in vivo animal models to validate the functional roles and mechanisms of action of these key genes, forming a strong foundation for a deeper understanding of the molecular mechanisms underlying GAC lymph node metastasis.

Methods

Ethical approval

This study has obtained approval from the Experimental Animal Welfare and Ethics Committee of the Second Affiliated Hospital of Kunming Medical University (Approval No.: kyfey2025041) and the Medical Ethics Committee of the Second Affiliated Hospital of Kunming Medical University (Review Date: August 22, 2022; Approval Date: August 30, 2022; Approval No.: Shen-PJ-Ke-2022-159). All experimental procedures in this study were conducted in accordance with the principles of the Declaration of Helsinki. Written informed consent was obtained from all participants prior to sample collection.

scRNA-seq and data processing

scRNA-seq data (GSE234129) **were retrieved** from the Gene Expression Omnibus (GEO, https://www.ncbi.nlm.nih.gov/geo/). This study's analysis covers all sample types within the GSE234129 dataset. Single-cell dataset objects were constructed using the Seurat software package (v5.3.0), upon which subsequent quality control and downstream analyses were carried out. First, the gene-barcode matrix was imported into the R programming language, with the Seurat software package (v5.3.0) serving as the core analytical tool. A series of analyses including quality control, data normalization, data scaling,

dimensionality reduction, cell clustering and visualization were sequentially performed. To eliminate the interference of technical factors such as sequencing depth differences and cell cycle heterogeneity, and to avoid the generation of false-positive signals of biological differences, a standardized analytical strategy was adopted subsequently. The workflows of the NormalizeData and ScaleData functions built in the Seurat software were utilized to sequentially implement data normalization and scaling. Further, data correction was conducted using the Harmony algorithm.

The detailed procedures are described as follows: Principal component analysis (PCA) was performed on the scaled data via the RunPCA function, and the top 50 principal components were extracted to capture core biological information. Subsequently, the IntegrateLayers function was invoked to run the Harmony algorithm based on the aforementioned 50 principal components for sample integration, generating a corrected Harmony dimensionality reduction matrix, which was employed for subsequent cell clustering and visualization analyses. On the basis of the integrated Harmony dimensionality reduction data, unsupervised cell clustering analysis was performed. The FindNeighbors function was used to construct a shared nearest neighbor (SNN) graph based on the top 30 Harmony dimensions, thereby accurately capturing the potential biological associations among cells. Then, the FindClusters function was adopted, combined with a modularity optimization clustering algorithm based on the SNN graph, to perform unsupervised clustering of cell populations and achieve objective cell grouping. Finally, uniform manifold approximation and projection (UMAP) dimensionality reduction analysis was implemented via the RunUMAP function based on the same top 30 Harmony dimensions, which projected high-dimensional single-cell data into a two-dimensional space and accomplished the visualization of cell clustering results.

Patient samples

5 patients diagnosed with GAC by experienced pathologists and radiologists were enrolled in this study. A total of 8 fresh biopsy samples were obtained, including 2 Primary lesions (PL), 3 metastatic Primary lesions (MPL), and 3 metastatic lymph nodes. These samples were designated as PL-1、PL-2、MPL-1、MPL-2 、MPL-3, MLN-1、MLN-2 and MLN-3, respectively, and used for ST sequencing and subsequent analysis. LNM was confirmed by pathological assessment via intraoperative cytological examination and postoperative paraffin-embedded sections. Patient demographics and tumor clinicopathological characteristics are detailed in Supplementary Material 1.

Human tissue preparation

Following tumor tissue isolation from eight fresh biopsy samples, blood and connective tissue were immediately removed, and the tissue was rapidly frozen on dry ice. The tumor tissue was then cross-sectionally cut and embedded in optimal cutting temperature (OCT) compound for ST analysis.

ST and data processing

The spatial transcriptome sequencing procedures were mainly carried out by Chongqing Biomedicine Biotech Co., Ltd. Specifically, the Visium Spatial Gene Expression technology was employed to analyze the tissue sections. Firstly, the frozen sections were cut to a thickness of 10 μm and mounted on the GEX array, and then the mounted sections were placed on the thermal cycler adapter. Subsequently, the sections were fixed with methanol at -20 °C for 30 min and stained with hematoxylin and eosin (H&E) (Eosin, Dako CS701; Hematoxylin, Dako S3309; Bluing Buffer, Dako CS702). The bright-field images were acquired with a Leica DMI8 whole-slide scanner at a 10× resolution. Then, according to the protocol provided by 10x Genomics (https://10xgenomics.com/), the Visium Tissue Optimization and Spatial Gene Expression experiments were performed with H&E as the counterstain. The tissue sections were processed using the Visium Spatial Gene Expression Slides and Kit (10x Genomics, PN-1000184). A leak-proof well was constructed using the slide box, and 70 μL of permeabilization enzyme was added and incubated at 37 °C for 12 min for optimal permeabilization. After permeabilization, the sections were washed with 100 μL of SSC, and 75 μL of reverse transcription master mix was added to synthesize cDNA. Upon the completion of the first-strand synthesis, the RT master mix in the well was removed, 75 μL of 0.08 M KOH was added and incubated at room temperature for 5 min, followed by washing with 100 μL of EB buffer. Thereafter, 75 μL of the second-strand mix was added to each well for the second-strand synthesis, and the cDNA was amplified on the S1000 Touch Thermal Cycler (Bio-Rad). Finally, the Visium Spatial Library was constructed using the Visium Spatial Library Construction Kit (10x Genomics, PN-1000184) and sequenced on the Illumina NovaSeq 6000 sequencer with a sequencing depth of at least 100,000 reads per spot and a paired-end 150 bp (PE150) reading strategy. The STUtility spatial transcriptome analysis toolkit was used to preprocess the measured expression profile data and the corresponding HE-stained images, and the connective tissue area, muscle area, and tumor area were annotated on the samples based on the histological location and boundaries. After the completion of quality control and data normalization operations, PCA was performed on the highly variable genes (HVG), and 30 dimensions were selected by default

for clustering. The spatial transcriptome sequencing data of each sample were integrated using the sctransform method of Seurat v5 software, and the clustering results were visualized by the UMAP method.

Construction of marker gene set for tumor epithelial cells

A tumor epithelial cell-specific marker gene set was constructed, which includes epithelial cell core markers previously validated in the literature: EPCAM (epithelial cell adhesion molecule), KRT8 (keratin 8), CEACAM6 (carcinoembryonic antigen-related cell adhesion molecule 6), CDH1 (cadherin 1), REG4 (regenerating family member 4), and CLDN4 (claudin 4). Based on this gene set, gene set enrichment scores were calculated for each sequencing spot in the spatial transcriptomic data using the AddModuleScore function of Seurat v5 software.

Cell type deconvolution analysis

The Robust Cell Type Decomposition (RCTD) algorithm was employed to perform cell type deconvolution for spatial transcriptome spots, with paired scRNA-seq data serving as the reference. First, a reference dataset was constructed based on the raw count matrix and cell type annotations derived from scRNA-seq data. Subsequently, the gene expression profiles and spatial coordinates within the tissue-covered regions of spatial transcriptome samples were extracted, and the full doublet mode (doublet mode = 'full') of RCTD was executed to infer the relative abundances (Weights) of distinct cell types at each spatial spot. Finally, the cell type with the highest weight at each spot was defined as its dominant type, and all deconvolution results were integrated into the Seurat object for subsequent spatial visualization and microenvironment analysis.

Gene ontology (GO) functional enrichment analysis

GO functional enrichment analysis was performed using the R package clusterProfiler. Enrichment analyses were conducted from three dimensions, including Biological Process (BP), Cellular Component (CC), and Molecular Function (MF). The threshold for significant enrichment was set as P-value < 0.05 and false discovery rate (FDR) < 0.1. Finally, the core functional terms of proliferative B cells were obtained.

Screening of key genes

Gene expression data of proliferative B cells were collected. A LASSO regression model was constructed using the R package "glmnet". The optimal penalty parameter λ was determined via 10-fold cross-validation. Genes with non-zero coefficients were screened out based on this model, and the number of retained genes in proliferative B cells was recorded. Using the gene expression data after screening, a random forest model was built with the R package "randomForest". The importance score of each gene was calculated using either the mean decrease in Gini impurity or the mean decrease in accuracy. Based on the prediction results of the random forest model, the receiver operating characteristic (ROC) curve was plotted using the "pROC" package in R software (Version 4.0.1; R Core Team; Official website: http://www.r-project.org).

Analysis of PAX5 expression at the spatial transcriptomic level

Normalized expression values of the PAX5 gene corresponding to spots in the PL, MPL, and MLN regions were extracted from spatial transcriptomic annotation results using the STUtility package (v1.1.0). Low-quality spots within each region were excluded. The median expression level, quartiles, and range of PAX5 in each sample group were calculated using the R package dplyr. This was performed to clarify the characteristics of intergroup expression differences. The Kruskal-Wallis H rank sum test, a non-parametric test method, was employed to compare the overall differences in PAX5 expression levels among the three groups. Dunn's method was used for multiple intergroup comparisons to control Type I error. Violin plots were generated using the R package ggplot2 to visualize the results.

Cell culture

Frozen SGC-7901 cells (FH0264, FuHeng BioLogy, Shanghai, China) were retrieved from liquid nitrogen or a -80 °C freezer and rapidly thawed by agitation in a 37 °C water bath. The thawed cell suspension was transferred to a centrifuge tube containing 5 mL of complete culture medium and centrifuged at 1000 rpm for 5 min. The supernatant was discarded, and the cells were resuspended in 4–6 mL of complete culture medium. The cell suspension was then seeded into a T25 flask or 6 cm culture dish and incubated overnight. The culture medium was changed, and cell density was assessed the following day. When cell density reached 80%-90%, cells were passaged. The culture supernatant was removed, and the cells were rinsed with calcium- and magnesium-free PBS once or twice. Subsequently, 1–2 mL of trypsin-EDTA solution (0.25% Trypsin-0.53mM EDTA) was added to the flask, and the cells were incubated at 37 °C for 3–5 min, with cell detachment monitored microscopically. Once most cells had rounded up and detached, the flask was removed, tapped gently, and 5 mL or more of complete culture medium containing 10% serum was added to halt digestion. The cells were gently pipetted to detach completely, transferred to a centrifuge tube, and centrifuged at 1000 rpm for 5–8 min. The supernatant was discarded, and the cells were resuspended in 1–2 mL of complete culture medium. The cell suspension was

then split at a 1:2 ratio into new culture dishes or flasks, and 5–6 mL of complete culture medium was added.

Transfection of SGC-7901 cells

The oe-NC, oe-PAX5, sh-NC, and sh-PAX5 plasmids were generated by General Biosystems (Anhui) Co., Ltd. SGC-7901 cells were seeded in 10 cm culture dishes at a density of 5 × 10^6 cells per dish. For each transfection, 10 μg of the appropriate plasmid (oe-NC, oe-PAX5, sh-NC, or sh-PAX5) was dissolved in 490 μL of Opti-MEM™ (31985070, Gibco, California, USA), gently mixed, and incubated at room temperature for 5 min. Concurrently, 30 μL of transfection reagent (16447100, Thermo, Waltham, Massachusetts, USA) was dissolved in 470 μL of Opti-MEM™, gently mixed, and incubated at room temperature for 5 min. The transfection reagent mixture was then added to the corresponding plasmid solution, thoroughly mixed, and incubated at room temperature for 15 min to form transfection complexes. Following three cycles of pipetting with a 1 mL pipette tip, the transfection complexes were evenly added to the culture dishes, mixed using a crosshatch pattern, and incubated. After 6 h, the medium was replaced with fresh complete culture medium, and cells were harvested after 48 h. Finally, cells were categorized into the oe-NC, oe-PAX5, sh-NC, and sh-PAX5 groups.

Cell viability assay

Cell viability was assessed using the Cell Counting Kit-8 (CCK-8) assay kit, according to the manufacturer's instructions (C0038, Beyotime, Shanghai, China). Absorbance was measured at 450 nm using a microplate reader (CMax Plus, Molecular Devices, Sunnyvale, California, USA), and cell viability was calculated for each group as directed.

Cell migration assay

First, parallel horizontal lines were marked on the underside of 6-well plates, spaced 1 cm apart and traversing each well, with three lines per well. Cells in logarithmic growth were then selected. Approximately 1 mL of 0.25% trypsin solution was added to a T25 flask, swirled to coat the cells, and incubated at 37 °C for ~ 2 min. Once cells had rounded up or begun to detach, the flask was gently agitated to detach all cells, and 2 mL of complete culture medium was added. After gentle trituration and the addition of RPMI-1640 complete culture medium (L210KJ, BaseMedia, Shanghai, China), the cell suspension was adjusted to a density of 5 × 10^5 cells/well, seeded into 6-well plates, and incubated at 37 °C in a 5% CO2 atmosphere. Upon reaching 90% confluence, the original medium was aspirated, the cells were rinsed three times with PBS, and then 1 mL of PBS was added to each well. A scratch was then made across the well using a 10 μL pipette tip, followed by two washes with PBS to remove detached cells. The initial scratch was imaged at 0 h using a microscope, and the cells were treated according to their respective groups and incubated at 37 °C in a 5% CO2 environment. After 24 h, cell migration was assessed by imaging under a microscope (CKX3-SLP, OLYMPUS, Tokyo, Japan). Migration distances were measured with ImageJ (Fiji, National Institutes of Health, America; download site: https://imagej.net/ij/download.html), and migration rates were calculated using the formula: migration rate = (initial scratch area - final scratch area) / initial scratch area × 100%.

Cell invasion assay

Matrigel (3422, Corning, New York, USA) was placed at 4 °C overnight (24 h) to liquefy. Subsequently, serum-free culture medium and Matrigel were mixed thoroughly at a 5:1 ratio. Following mixing, 100 μL of the mixture was added to the upper chamber of Transwell inserts (354234, Corning, New York, USA) to allow the Matrigel to solidify. Cells were then adjusted to a density of 5 × 10^5 cells/mL and added to the solidified Matrigel after a wash with serum-free medium. The lower chamber was filled with 500 μL of conditioned medium supplemented with 20% FBS, and the cells were incubated for 24 h at 37 °C in a 5% CO2 atmosphere. After incubation, the Transwell inserts were removed, the medium in the wells was discarded, and the cells were washed twice with calcium-free PBS. The cells were then fixed with 4% paraformaldehyde for 20 min, washed with PBS, and stained with 0.1% crystal violet solution (G1062, Solarbio, Beijing, China) for 20 min. Finally, cells were counted in randomly selected fields using a microscope, and the average.

Immunofluorescence staining

Fixed cell slides were washed three times with PBS. Slides were then blocked with goat serum for 1 h at room temperature and subsequently incubated overnight at 4 °C with Rabbit Anti-PAX5 antibody (bsm-60221R, Bioss, Beijing, China) at a 1:100 dilution. Following three washes with PBS, the slides were incubated with a secondary antibody (GB22403, Servicebio, Wuhan, China) at a 1:200 dilution for 1.5 h in the dark at room temperature. After incubation, the slides were washed three times for 5 min each with PBS. DAPI (C1005, Beyotime, Shanghai, China) was added for a 5-minute incubation in the dark, followed by washes with PBS to remove excess DAPI. Finally, the slides were mounted with an antifade mounting medium (P0126, Beyotime, Shanghai, China). Images were acquired using a microscope (MF53, Mshot, Guangzhou, China). DAPI-stained nuclei appeared blue, and FITC signals appeared green.

Real-time quantitative polymerase chain reaction (RT-qPCR)

Total RNA was extracted from samples using the TRIzol method, and RNA concentrations were quantified using spectrophotometry. RNA was reverse transcribed to cDNA using the Goldenstar™ RT6 cDNA Synthesis Kit Ver.2 (TSK302M, Tsingke, Beijing, China), and qPCR was performed using 2 × T5 Fast qPCR Mix (SYBR Green I) (TSE202, Tsingke, Beijing, China). GAPDH was used as an endogenous control, and relative gene expression was calculated using the $2^{-\triangle\triangle Ct}$ method. Specific gene primer sequences are shown in Table 1.

Western blotting

Total protein was extracted from cells using RIPA lysis buffer supplemented with PMSF (ST507, Beyotime, Shanghai, China) and a protease inhibitor cocktail (P1045, Beyotime, Shanghai, China). Five hundred micrograms of total protein were mixed with 5× SDS loading buffer (8015011, DAKEWE, Shenzhen, China) at a 4:1 ratio and heated at 100 °C for 6 min. Sixty micrograms of denatured protein were loaded. Electrophoresis was performed with an initial run at 80 V through the stacking gel, followed by 120 V until the bromophenol blue reached the bottom of the gel. A sponge pad, filter paper, the gel, and PVDF membrane were layered, and transfer buffer was introduced. Protein was transferred at a constant current of 250 mA, with the transfer time determined by the molecular weight of the target protein. Following transfer, the membrane was removed, and both sides were marked. The membrane was washed with TBST for 1 min. Then, the membrane was blocked with 5% skim milk (P0216, Beyotime, Shanghai, China) for 1 h, and subsequently washed three times with TBST for 5 min each. The primary antibody was diluted 1:1000 and incubated at 4 °C overnight. The secondary antibody (AS014, Abclonal, Wuhan, China) was diluted 1:2000 and incubated at room temperature for 1 h. After all incubations, the membrane was covered with a mixture of ECL substrate (34580, Thermo, Waltham, Massachusetts, USA) and allowed to react for 1 min before detection using a nucleic acid protein gel imaging system (Universal Hood II, Bio-Rad, California, USA). Protein band images were then analyzed using ImageJ software (version 1.8.0; download site: https://imagej.en.softonic.com/download). Antibody details are as follows: PAX5 (A12048, ABclonal, Wuhan, China), VEGF-C (A2556, ABclonal, Wuhan, China), AKT1 (A17909, ABclonal, Wuhan, China), PI3K (A19742, ABclonal, Wuhan, China), MMP2 (A19080, ABclonal, Wuhan, China), and Ki-67 (A16919, ABclonal, Wuhan, China). GAPDH (GAPDH, ABclonal, Wuhan, China) served as an endogenous control protein.

Table 1 Primer sequences used in qPCR

Primer name(s)	Sequences
PAX5-F	CTTGCTCATCAAGGTGTCAGGC
PAX5-R	TGGCGACCTTTGGTTTGGATCC
VEGF-C-F	GCCAATCACACTTCCTGCCGAT
VEGF-C-R	AGGTCTTGTTCGCTGCCTGACA
PI3K-F	TCAGCAGCCAGCTCTGATAAT
PI3K-R	TACCAAAAAGGTCCCGTCTG
AKT1-F	TGGACTACCTGCACTCGGAGAA
AKT1-R	GTGCCGCAAAAGGTCTTCATGG
GAPDH-F	GTCTCCTCTGACTTCAACAGCG
GAPDH-R	ACCACCCTGTTGCTGTAGCCAA

Co-culture of transfected SGC-7901 and HLEC cells

The oe-PAX5 and sh-PAX5 plasmids were generated by General Biosystems (Anhui) Co., Ltd, and SGC-7901 cells were transfected as previously described. A co-culture system was established using Transwell inserts to simulate the in vivo environment. SGC7901 cells were placed in the upper chamber (cell concentration: 1 × 10^5 cells/mL), while HLEC cells (FH1250, FuHeng BioLogy, Shanghai, China) were placed in the lower chamber, pre-coated with Matrigel (cell concentration: 5 × 10^4 cells/mL). Co-culture was performed under the same conditions to facilitate cell-cell interaction. Control HLEC cells were cultured alone. Finally, cultured cells were divided into Control, oe-NC, oe-PAX5, sh-NC, and sh-PAX5 groups.

Tube formation assay

Following 48 h of co-culture, endothelial cell node numbers and total length of major master segments were quantified in randomly selected fields using a 100× microscope (BLD-200, KEXIN, Shanghai, China) and analyzed with ImageJ software (version 1.8.0; download site: https://imagej.en.softonic.com/download).

Animal modeling

Female BALB/c-nu (SPF) nude mice, 4–6 weeks old and weighing 15–18 g, were obtained from Chongqing Ensiweier Biotechnology Co., Ltd. All mice were housed under specific pathogen-free conditions: temperature of 23 ± 2 °C, humidity of 35–60%, and a 12 h light/dark cycle. Mice had ad libitum access to food and water and were acclimatized for one week at 23–25 °C before the start of the experiment. SGC-7901 cells (concentration: 5 × 10^7/mL) were drawn into a disposable syringe, and 200 μL of cell suspension was injected subcutaneously into the bilateral axillary and flank regions of nude mice. These mice were designated as the first generation of tumor-bearing nude mice and used for subsequent xenografting. Subcutaneous injections were repeated weekly until tumors developed. Subcutaneous tumors from stably tumorigenic sixth-generation tumor-bearing nude mice were used as the tumor source. Approximately two weeks following tumor tissue implantation, when

subcutaneous tumors reached a volume of 50–100 mm^3 (approx. 5 mm in diameter), shRNA mixture was injected peritumorally (5 mm away from the tumor) and intratumorally (multiple sites injected slowly). Each mouse received 25 μL of the shRNA/oligofectamine mixture at a dose of 1.00E + 09 pfu/mL, with injections repeated every four days for a 4-week tumor treatment study, after which the mice were euthanized and in situ tumor specimens collected.

Hematoxylin-eosin (HE) staining

Paraffin sections were prepared from in situ tumor specimens. Following deparaffinization and rehydration, sections were stained with hematoxylin solution (G1004, Servicebio, Wuhan, China) for 5 min, rinsed with distilled water, and subsequently stained with eosin solution (G1002, Servicebio, Wuhan, China) for 2 min. The sections were then dehydrated using a graded series of ethanol, cleared with xylene for 5 min, and mounted with neutral resin (10004160, Sinopharm, Beijing, China). Images were acquired with an Mshot MF53 microscope (Guangzhou Mshot Photoelectric Technology CO., Ltd.).

Immunohistochemistry (IHC)

Antigen retrieval was performed on deparaffinized and rehydrated paraffin sections by heat-induced epitope retrieval for 30 min. Specimens were treated with 3% hydrogen peroxide and then washed three times with PBS for 5 min each. Specimens were blocked with goat serum (C0265, Beyotime, Shanghai, China) for 1 h. This was followed by incubation with primary antibody overnight at 4 °C. Subsequently, specimens were incubated with the secondary antibody at a 1:200 dilution for 1.5 h at room temperature. Following incubation, DAB (ZLI-9019, ZSGB-BIO, Beijing, China) was used for color development in the dark for 1 min. To provide counterstaining, specimens were stained with hematoxylin (G1004, Servicebio, Wuhan, China) for 1 min and then differentiated with 1% hydrochloric acid in ethanol for 2 s. After differentiation, specimens were rinsed with tap water to restore the blue color. Sections were then dehydrated with 95% ethanol for two minutes, followed by a second dehydration with fresh 95% ethanol for two minutes. The sections were then cleared with xylene for 5 min, followed by a second clearing with fresh xylene for 5 min. Finally, sections were mounted with neutral resin (10004160, Sinopharm, Beijing, China). Images were then acquired under a microscope (MF53, Mshot, Guangzhou, China). Cell nuclei appeared blue, while positive staining was indicated by a brown-yellow color. Antibody details are as follows: Anti -Ki67 Mouse mAb (GB121141-100, Servicebio, Wuhan, China), Anti -MMP2 Rabbit pAb (GB11130-100, Servicebio, Wuhan, China), PAX5 Recombinant Rabbit mAb (bsm-60221R, Bioss, Beijing, China), Goat Anti-Rabbit HRP IgG H&L (HRP) (511203, ZEN-BIOSCIENCE, Chengdu, China), and Goat Anti-Mouse HRP IgG H&L (HRP) (511103, ZEN-BIOSCIENCE, Chengdu, China).

Statistical analysis

Experimental data were analyzed using GraphPad Prism version 8.0.1 (GraphPad Software, USA, download site: https://www.graphpad-prism.cn). Assembly of the figures was conducted using Adobe Illustrator 2021 software. Data are presented as mean ± standard error of the mean (SEM). Comparisons between groups were performed using one-way ANOVA and t-tests. All experiments were performed in at least triplicate. Statistical significance was defined as $P < 0.05$.

Results

Single-cell atlas of lymph node cells in GAC

To systematically characterize the cellular composition and structural features of GAC lymph nodes, scRNA-seq technology on the 10x Genomics platform was employed (Fig. 1A). scRNA-seq data were rigorously filtered to exclude damaged cells, dead cells, and suspected doublets. After quality control, a total of 19,488 cells were retained for subsequent analyses. Cells in this dataset were colored according to their annotated cell types. Through this approach, eight distinct cell types were identified (Fig. 1B), including T cells (n = 9329), natural killer (NK) cells (n = 2,968), B cells (n = 876), plasma cells (n = 1,225), myeloid cells (n = 3,792), dendritic cells (n = 470), stromal cells (n = 411), and a unique proliferative cell cluster (n = 417). It is worth noting that the dataset was derived from lymphoid tissues associated with gastric adenocarcinoma and, as confirmed by original literature and official annotations, was verified to contain only immune cells and stromal cells with the absence of tumor cells [14].

Meanwhile, the characteristic genes corresponding to the aforementioned 8 cell types were screened out in the present study, and it was revealed by the results that each cell type exhibited a distinct gene expression profile (Fig. 1C, D). Specifically, genes such as CXCL13 and FOXP3 were highly expressed in T cells; KLRF1 was identified as the signature gene of NK cells; TCL1A was highly expressed in B cells; genes including IGLV3-25 and IGKV2-30 were found to be enriched in plasma cells; F13A1 was highly expressed in myeloid cells; CD1CD was recognized as the marker gene of dendritic cells; genes such as PTGDS and DMKN were highly expressed in stromal cells; proliferation-related genes (e.g., HMGB2, STMN1) were highly expressed in this proliferative cell cluster, which was also observed to form an independent cluster in the UMAP dimensionality reduction plot (Fig. 1E).

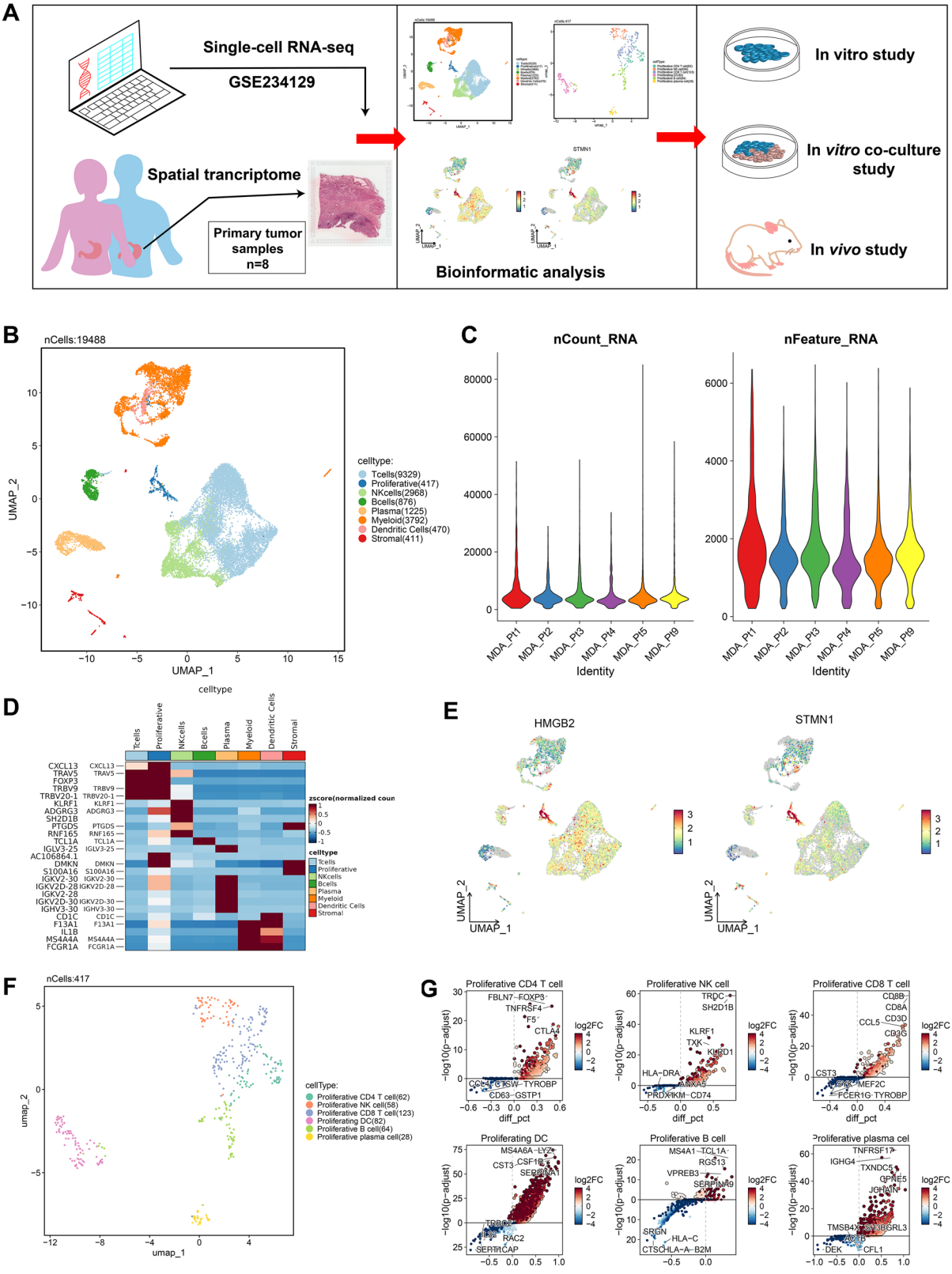

Fig. 1 Single-cell landscape of GAC. **A**. Schematic of the study workflow. **B**. UMAP visualization of 19,488 high-quality single cells. **C**. Distribution of QC metrics across patients. **D**. Dot plot of marker gene expression. **E**. Feature plots displaying the expression distribution of proliferation markers projected onto the UMAP embedding, confirming the identity of the proliferative cluster. **F.** Sub-clustering analysis of the "Proliferative" population ($n = 417$) identified in panel **B**. **G**. Volcano plot of differentially expressed genes

Further analysis of this proliferative cell cluster was performed via subcluster clustering (Fig. 1F-G). It was found that this proliferative cluster was not composed of a single cell type but consisted of multiple distinct proliferative subpopulations. These subpopulations included proliferative CD4 T cells ($n = 62$), proliferative NK cells ($n = 58$), proliferative CD8 T cells ($n = 123$), proliferative dendritic cells ($n = 82$), proliferative B cells ($n = 64$), and proliferative plasma cells ($n = 28$).

GO functional enrichment analysis and identification of key genes in proliferative B cells

Genes including 'EPCAM', 'KRT8', 'CEACAM6', 'CDH1', 'REG4', and 'CLDN4' were used as the marker gene set for tumor epithelial cells. Each spot in the spatial transcriptomic data was scored to identify tumor regions. Subsequently, the eight cell types identified by scRNA-seq were deconvoluted onto the spatial transcriptomic map of GAC tissue samples. A comprehensive cell abundance distribution map was obtained (Supplementary Material 2). Results showed that regions with aggregated T cells and B cells were observed in the tumor area of each sample, forming tertiary lymphoid structures (TLS). Meanwhile, the proliferative subpopulations identified by scRNA-seq were deconvoluted back into the spatial transcriptomic data. It was found that proliferative B cells were also aggregated in the TLS (Supplementary Material 3).

Based on the aforementioned findings, the spatial architecture and maturity of TLSs within the tumor microenvironment of gastric adenocarcinoma patients were further characterized via module score analysis: TLS signature scores for all spatial spots were calculated through the integration of canonical TLS signature gene sets, and the spatial colocalization relationships between this score and proliferative B cells, proliferative T cells as well as plasma cells were systematically evaluated. Quantitative correlation analysis revealed that the highest Pearson correlation coefficient was observed between proliferative B cells and the functional TLS signature score (Fig. 2A). Further validation was conducted using spatial signature profiles (Supplementary Material 4), demonstrating that, in contrast to diffusely distributed proliferative T cells, proliferative B cells were strictly confined to the core regions with high TLS scores, which indicates that they can serve as the most specific spatial indicators for functional TLSs.

Furthermore, GO functional enrichment analysis was performed on proliferative B cells (Figs. 2B-D). At the PL stage (Fig. 2B), proliferative B cells were mainly enriched in "apoptosis-related processes" (e.g., Apoptotic DNA fragmentation, DNA catabolic process) and "regulation of osteoclast differentiation". This suggested that proliferative B cells at this stage might participate in the early clearance of tumor cells by regulating cell apoptosis, or indirectly modulate tumor invasiveness by affecting osteoclast differentiation. At the MPL stage (Fig. 2C), their functions shifted to immune regulation processes such as "T cell differentiation" and "Natural killer cell activation". This indicated that with tumor progression, proliferative B cells gradually transitioned from direct cytotoxic effects to the regulation of adaptive immunity. They enhanced anti-tumor immune responses by promoting the activation of effector T cells and NK cells. At the MLN stage (Fig. 2D), an immune escape network was established through multiple abnormal functional changes. At the BP level, interleukin 4 production mediated T helper 2 (Th2)-type immune deviation. This was accompanied by the dysregulation of "Regulation of immune effector process" and "Somatic diversification of immune receptors", abnormal activation of "Negative regulation of lymphocyte migration" and "Complement dependent cytotoxicity". At the MF level, pro-tumor pathways and epigenetic reprogramming were regulated through "Tumor necrosis factor receptor binding" and other mechanisms. Combined with metabolic adaptation mediated by "G protein coupled purinergic nucleotide receptor activity", pro-tumor signals were amplified. At the CC level, the formation of a pro-tumor positive feedback loop was supported by competitive inhibition of the "T cell receptor complex" and long-range communication via "Blood microparticle", relying on the "Plasma membrane signaling receptor complex". Eventually, proliferative B cells were transformed into key effector cells driving immune suppression and metastasis.

Further LASSO regression analysis was conducted on the proliferative B cell population (Figs. 2E-F). Results showed that approximately 5 genes were screened out from proliferative B cells. Subsequently, a random forest model was constructed for proliferative B cells (Figs. 3G-I). Results indicated that PAX5 was a highly significant gene for predicting proliferative B cell-related characteristics. Although the AUC of this model was 0.736, which required further optimization to improve accuracy, it still possessed research value. Meanwhile, the expression and distribution of PAX5 in tissue sections of PL, metastatic MPL, and MLN were detected (Figs. 2J-K). The highest PAX5 expression level was observed in MLN, followed by MPL, and the lowest in PL. Significant differences in PAX5 expression levels were found among the three groups of samples ($P < 0.0001$).

PAX5 promotes GAC malignancy by upregulating VEGF-C and the PI3K/AKT1 signaling pathway

To elucidate the functional role of PAX5, we generated oe-PAX5 and sh-PAX5 plasmids and transfected them into SGC-7901 cells. Cell proliferation assays revealed that PAX5 overexpression significantly enhanced

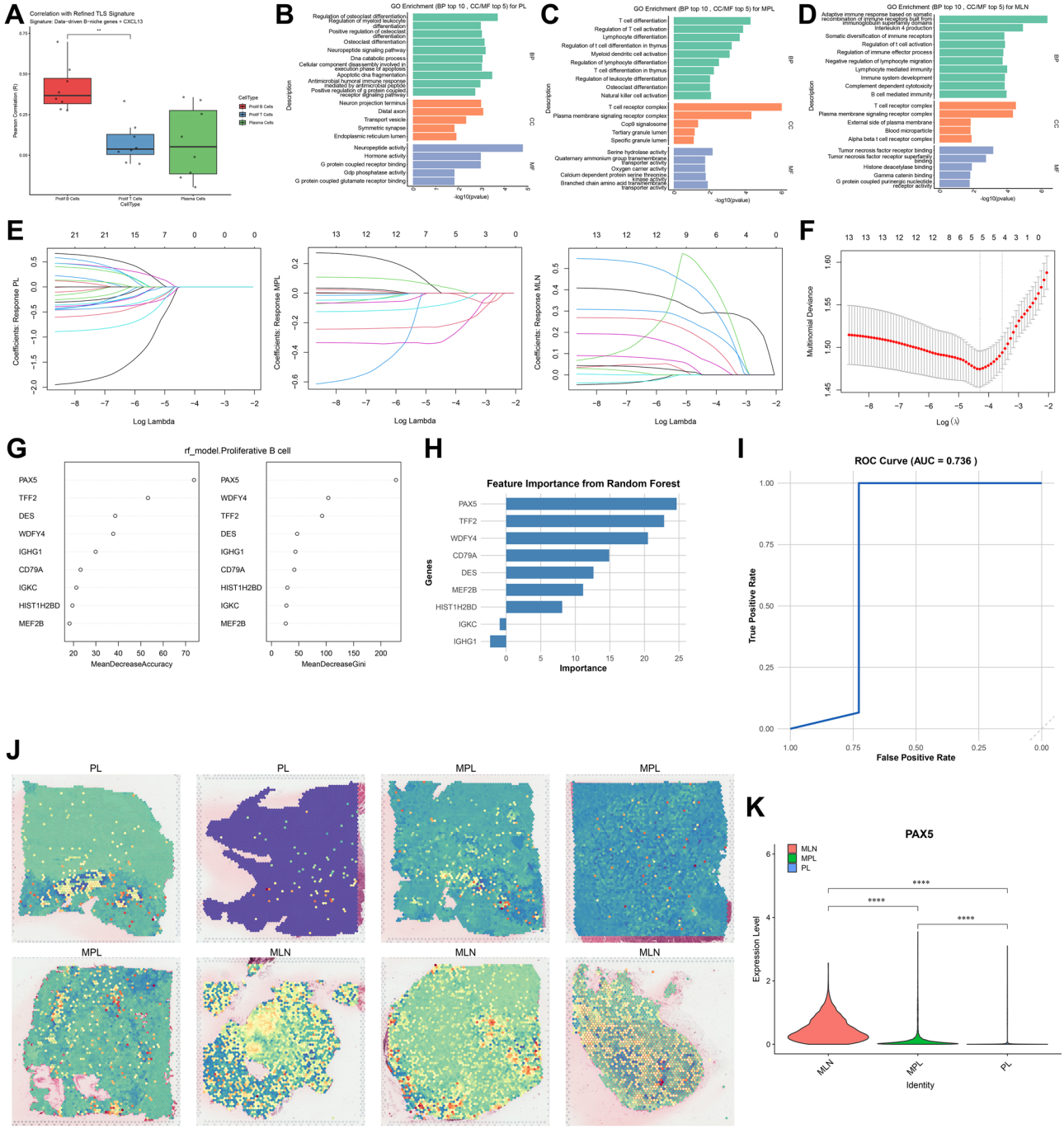

Fig. 2 GO functional enrichment analysis and identification of key regulatory genes in proliferative B cells. **A**. Spatial correlation analysis of immune cell subsets with the canonical tertiary lymphoid structure (TLS) signature. **B**. GO functional enrichment analysis of proliferative B cells in primary lesion samples. **C**. GO functional enrichment analysis of proliferative B cells in metastatic primary lesion samples. **D**. GO functional enrichment analysis of proliferative B cells in metastatic lymph node samples. **E**. LASSO regression coefficients of proliferative B cells among different sample types. **F**. Results of LASSO regression analysis for proliferative B cells. **G**. Random forest model plot of proliferative B cells. **H**. Top 20 genes ranked by feature importance in the random forest model for proliferative B cells. **I**. ROC curve of proliferative B cells. **J**. Spatial feature plot showing the expression distribution of PAX5 in tissue sections of PL, MPL, and MLN. **K**. Violin plot of PAX5 expression levels in spatial transcriptomic samples. ** indicates $P < 0.01$; **** indicates $P < 0.0001$

SGC-7901 cell viability (Fig. 3A, $P < 0.0001$), while PAX5 silencing markedly decreased cell viability ($P < 0.0001$). Cell migration and invasion assays (Fig. 3B-C, E) demonstrated that PAX5 overexpression promoted cell migration ($P < 0.01$) and invasion ($P < 0.001$), whereas PAX5 silencing reduced these abilities ($P < 0.01$). Immunofluorescence analysis (Fig. 3D-F) confirmed that PAX5 overexpression increased intracellular PAX5 fluorescence

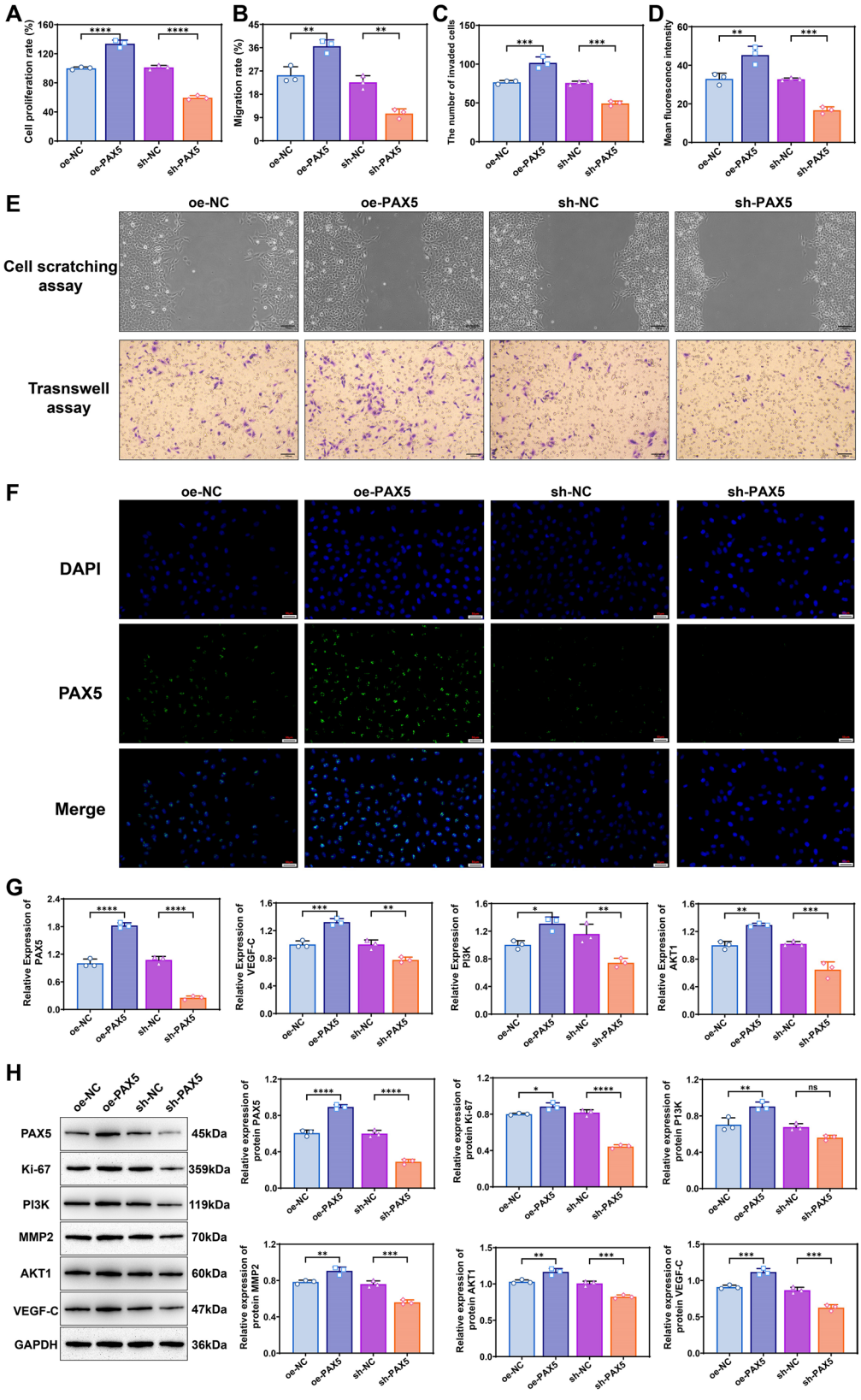

Fig. 3 (See legend on next page.)

(See figure on previous page.)

Fig. 3 PAX5 suppresses invasion and migration of GAC lymph node metastatic cells. **A**: CCK-8 assay measuring the viability of GAC lymph node metastatic cells. **B** and E: Scratch assay demonstrating cell migration; scale bar = 100 μm. **C** and F: Transwell assay assessing cell invasion; scale bar = 100 μm. **D** and **F**: Immunofluorescence analysis of PAX5 expression; scale bar = 50 μm. **G**: Quantitative PCR (qPCR) analysis of mRNA expression levels of PAX5, VEGF-C, PIK3, and AKT1. **H**: Western blot analysis of protein expression levels of PAX5, VEGF-C, AKT1, PI3K, MMP2, and Ki-67. "ns" indicates "not significant"; * indicates $P < 0.05$; ** indicates $P < 0.01$; *** indicates $P < 0.001$; **** indicates $P < 0.0001$

intensity ($P < 0.01$), while PAX5 silencing reduced the intensity ($P < 0.001$), validating effective PAX5 modulation by plasmid transfection. To further investigate the molecular mechanism underlying PAX5 action, we analyzed the expression levels of PAX5, VEGF-C, PI3K, AKT1, and proteins associated with cell proliferation and metastasis in SGC-7901 cells. Our findings (Fig. 3G-H) showed that PAX5 overexpression upregulated the mRNA and protein levels of PAX5, VEGF-C, PI3K, and AKT1 (all $P < 0.05$), while PAX5 silencing downregulated these factors (all $P < 0.01$). Moreover, PAX5 overexpression increased protein levels of MMP2 and Ki-67 (all $P < 0.05$), and PAX5 silencing decreased these protein levels (all $P < 0.001$). These results suggest that PAX5 promotes tumor cell proliferation and metastasis by modulating the VEGF-C and PI3K/AKT1 signaling pathways.

PAX5 enhances tumor angiogenesis

To mimic the in vivo environment and examine the role of PAX5 in tumor cell-vascular endothelial cell interactions and angiogenesis, we performed in vitro co-culture assays, combining SGC-7901 cells transfected with oe-PAX5 or sh-PAX5 plasmids with HLEC cells. Results showed that PAX5 overexpression significantly increased the number of nodes and total length of major segments in HLEC cells (Fig. 4A, $P < 0.01$ and $P < 0.05$, respectively), whereas PAX5 silencing markedly reduced these parameters ($P < 0.0001$). Concurrently, we assessed mRNA levels of *PAX5*, *VEGF-C*, *PIK3*, and *AKT1* in HLEC cells (Fig. 4B). These results revealed that PAX5 overexpression upregulated the expression of these genes (all $P < 0.01$), while PAX5 silencing downregulated their expression (all $P < 0.0001$). These findings suggest that PAX5 promotes tumor growth, potentially through the modulation of angiogenesis via the VEGF-C and PI3K/AKT1 signaling pathways.

PAX5 positively regulates its expression and the PI3K/AKT1 pathway in vivo

To further validate the role of PAX5 in vivo, we developed a subcutaneous tumor-bearing mouse model. HE staining of mouse tumor tissues revealed distinct morphological differences across treatment groups (Fig. 5A): oe-NC tumors displayed a scattered distribution of tumor cells, numerous bleeding points, sparse vacuolar structures, minimal cytoplasmic dissolution, and some nuclear condensation, fragmentation, and dissolution; oe-PAX5 tumors exhibited more prominent nucleolar hypertrophy, hemorrhage, and nuclear division, along with irregular cell morphology, variable cell sizes, tight cell packing, intense staining, coarse granular chromatin, and uneven chromatin distribution. sh-NC tumors presented a more dispersed tumor cell distribution with multiple bleeding points, minimal cytoplasmic dissolution, and some nuclear condensation, fragmentation, and dissolution. sh-PAX5 tumors displayed a scattered tumor cell distribution with reduced cell density, extensive hemorrhage, cytoplasmic dissolution, vacuolar structures, and extensive nuclear condensation, fragmentation, and dissolution. Immunohistochemical analysis (Fig. 5B) further demonstrated that PAX5 overexpression resulted in increased expression of PAX5, Ki-67, and MMP2 in mouse tumors ($P < 0.01$), whereas PAX5 silencing reduced their expression ($P < 0.05$). This reinforces the in vivo role of PAX5 in promoting tumor cell proliferation, consistent with the morphological features of active proliferation observed in the oe-PAX5 group in H&E staining. Furthermore, qPCR and WB analyses (Fig. 5C-D) showed that PAX5 overexpression upregulated the mRNA and protein levels of PAX5, PI3K, AKT1, and VEGF-C ($P < 0.05$), and conversely, PAX5 silencing downregulated these factors ($P < 0.05$). These data indicate that PAX5 positively regulates the expression of itself, and of genes and proteins associated with the PI3K/AKT1 signaling pathway (PI3K, AKT1), and positively modulates the expression of the angiogenesis-related factor, VEGF-C, in vivo.

Discussion

This study, integrating scRNA-seq, ST, cell biology, and in vivo animal models, elucidates the complexity of the GAC lymph node metastasis microenvironment and highlights the critical role of PAX5 in tumor cell proliferation, migration, invasion, and angiogenesis.

Lymph nodes, critical metastatic sites and immune hubs, possess complex cellularity influencing tumor progression and treatment respons [15]. In GAC lymph node samples, single-cell sequencing identified eight principal cell types. These encompassed T cells, NK cells, B cells, plasma cells, myeloid cells, stromal cells, and proliferative cell clusters, forming the core cellular framework of the GAC lymph node immune microenvironment. This composition is highly consistent with established gastric cancer immune microenvironment profiles [2].

Immune cell proliferation in the tumor microenvironment reflects immune response status, but prior studies

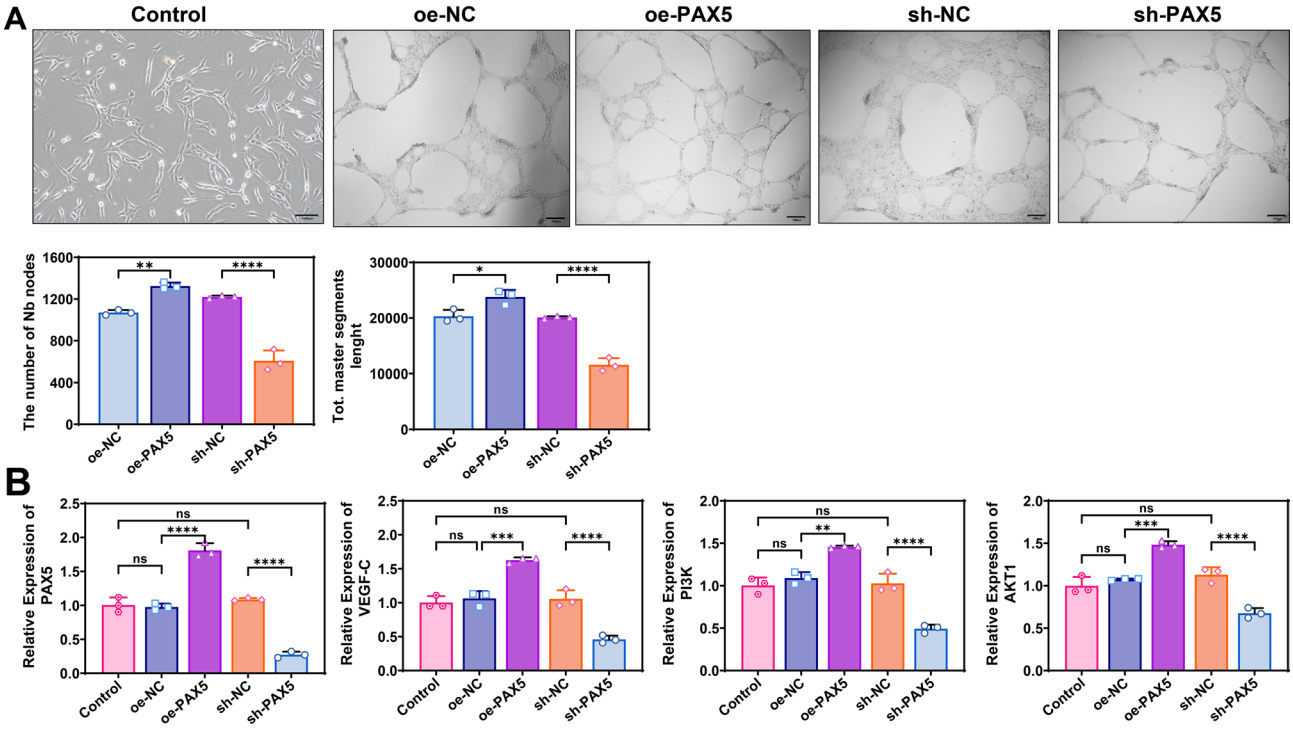

Fig. 4 PAX5 modulates HLEC cell tube formation in a co-culture system. **A**: Quantification of the number of nodes and total length of major master segments in tube-like structures. **B**: qPCR analysis of mRNA expression levels of PAX5, VEGF-C, PIK3, and AKT1 in HLEC cells. "ns" indicates "not significant"; * indicates $P < 0.05$; ** indicates $P < 0.01$; *** indicates $P < 0.001$; **** indicates $P < 0.0001$; scale bars = 100 μm

overlooked the heterogeneity of proliferative cell populations [16]. For the first time, a proliferative cluster, comprising six immune cell subpopulations (proliferative CD4 + T cells, CD8 + T cells, NK cells, B cells, plasma cells, and dendritic cells), was identified in GAC lymph nodes. This cluster exhibited high expression of proliferation markers like HMGB2 and STMN1. Widespread immune cell proliferation was observed in GAC lymph nodes, indicative of a dynamic tumor-immune balance. While immune cells proliferate to combat tumors, tumors may exploit this by inducing aberrant proliferation and functional remodeling for immune evasion or suppression [17].

Spatial transcriptomics analysis revealed TLS formation and proliferative B cell aggregation, a central discovery of this study. TLS are spontaneous lymphoid aggregates in the tumor microenvironment. Their presence correlates with improved patient prognosis by recruiting and activating immune cells to bolster local anti-tumor immunity [18]. Through spatial transcriptomic deconvolution analysis, it was first confirmed in this study that T cells and B cells exhibit a clustered distribution in the tumor regions of gastric adenocarcinoma (GAC) lymph nodes, where typical tertiary lymphoid structures (TLS) are formed. Furthermore, proliferative B cells are specifically enriched within these TLS—this finding reveals the core functional role of TLS in the immune microenvironment of GAC lymph nodes. Regarded as "immune response hubs" in the tumor microenvironment, TLS mediates the establishment of local anti-tumor immune responses. This is achieved through recruiting immune cells, promoting antigen presentation, and facilitating lymphocyte activation [19]. In the present study, the enrichment of proliferative B cells within TLS was suggested to indicate that the proliferation and differentiation of B cells may rely on the cytokine microenvironment and intercellular crosstalk provided by TLS. Within TLS, synergistic interactions between B cells and $CD4^+$ follicular helper (Tfh) cells drive germinal center reactions, through which high-affinity antibody-secreting plasma cells are generated. Meanwhile, B cells directly enhance $CD8^+$ T cell cytotoxic responses via antigen presentation and cytokine secretion [20]. This finding provides direct cytological evidence for the anti-tumor immune function of TLS in GAC lymph nodes.

B cells, as key mediators linking innate and adaptive immunity, are closely associated with tumor progression through their functional differentiation [21]. In the present study, GO functional enrichment analysis confirmed that proliferative B cells—critical connectors between innate and adaptive immunity—exhibit significant functional heterogeneity across different progression stages of GAC, including PL, MPL, and MLN. This heterogeneity reflects their characteristics of dynamic remodeling in

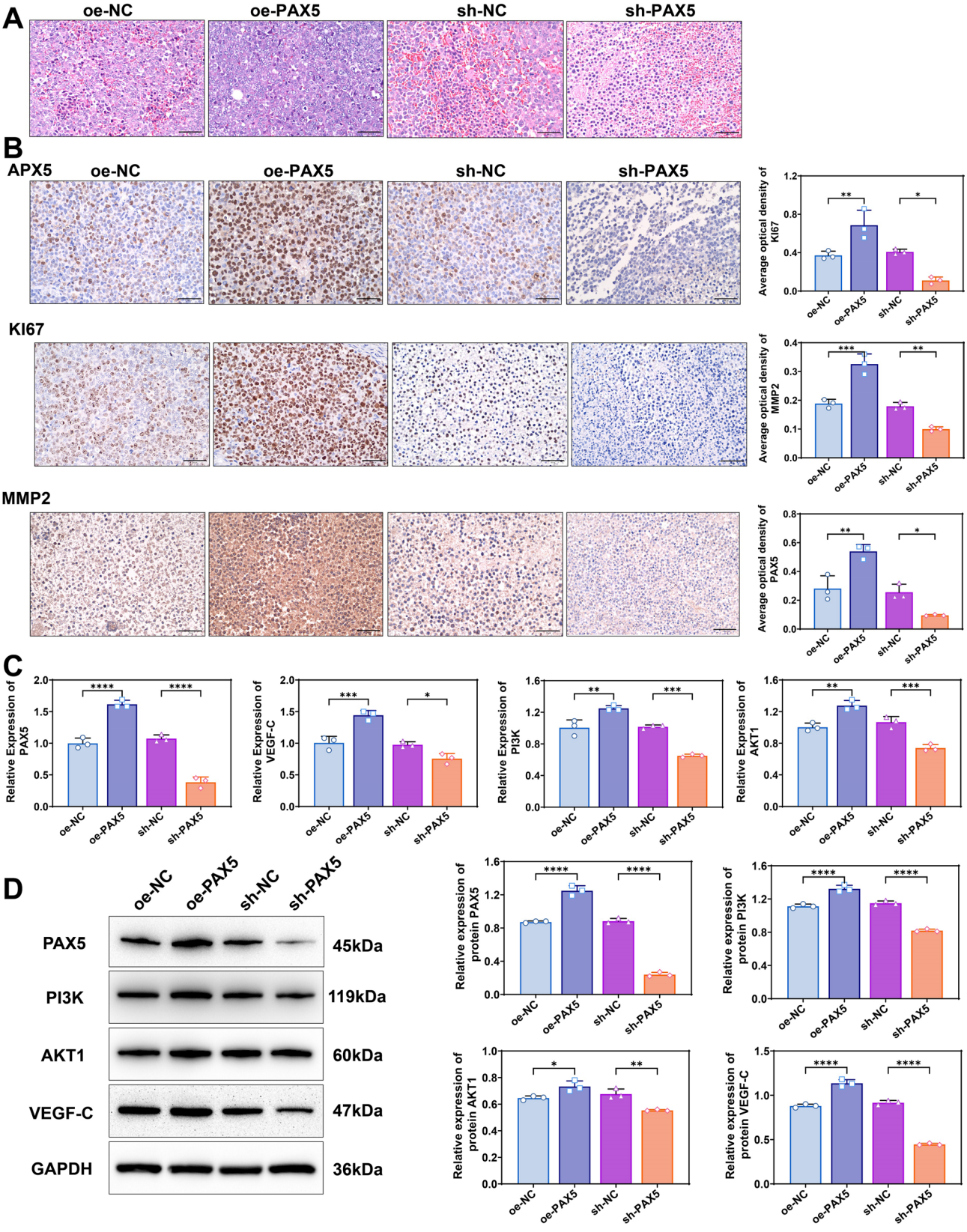

Fig. 5 In vivo validation of PAX5 functional mechanisms. **A**: Hematoxylin and eosin (H&E) staining of mouse tumors. **B**: Immunohistochemical analysis of PAX5, Ki-67, and MMP2 expression in mouse tumors. **C**: qPCR analysis of mRNA expression levels of PAX5, PIK3, AKT1, and VEGF-C in mouse tumors. **D**: Western blot analysis of protein expression levels of PAX5, PI3K, AKT1, and VEGF-C in mouse tumors. * indicates $P < 0.05$; ** indicates $P < 0.01$; *** indicates $P < 0.001$; **** indicates $P < 0.0001$; scale bars = 50 μm

the tumor immune microenvironment. At the PL stage, B cells focus on apoptosis regulation and osteoclast differentiation control, participating in early tumor clearance and invasion restriction. At the MPL stage, their function shifts to regulating the activation of immune cells such as T cells and NK cells, thereby enhancing anti-tumor immune responses. At the MLN stage, B cells establish an immune escape network through Th2-type immune deviation, dysregulation of immune effector processes, inhibition of lymphocyte migration, and abnormal activation of the complement pathway. Combined with the regulation of pro-tumor pathways, metabolic adaptation, and misleading intercellular signal transmission, they ultimately transform into key effector cells that drive immune suppression and tumor metastasis. A review by Wang et al. [22] clarified that B cells exhibit remarkable functional plasticity in the TME. For instance, anti-tumor immunity can be mediated by B cells through antibody secretion or activation of complement-dependent cytotoxicity (CDC) [23]. Additionally, B cells secrete effector cytokines (e.g., IFN-γ). These cytokines may skew T cell responses toward Th1 or Th2 phenotypes, or promote T cell responses by acting as antigen-presenting cells, thereby exerting negative regulatory effects on tumors [24].

PAX5, a core transcription factor regulating B cell development and function, plays an irreplaceable role in B cell proliferation, differentiation, and immunoglobulin gene rearrangement [25, 26]. Through Lasso regression and random forest model analysis in this study, PAX5 was identified as a highly significant gene predicting the characteristics of proliferative B cells. Its expression level was the highest in MLNs and the lowest in PLs, with extremely significant differences among the three groups. This finding suggests that PAX5 may be involved in the functional regulation of proliferative B cells and the lymph node metastasis process of GAC.

To delineate the specific role of PAX5 in GAC, we demonstrated through in vitro cell assays that PAX5 promotes the proliferation, migration, and invasion of GAC cells. These results align with previous findings linking PAX5 protein expression to neuroblastoma cell proliferation and its involvement in human growth hormone-induced breast cancer cell proliferation [27, 28]. Moreover, studies have established PAX5 as a regulator in several non-hematopoietic tissues and cancers, including malignant neuroblastoma and pediatric brain tumors, with its expression consistently promoting cell proliferation [29] These findings collectively support a similar pro-tumorigenic role for PAX5 in GAC. Additionally, we observed that PAX5 upregulates VEGF-C expression, thereby fostering tumor angiogenesis. VEGF-C, a critical mediator of neovascularization, is instrumental in tumor growth and metastasis [30]. Several studies have reported elevated VEGF-C expression across various malignancies, driving lymphangiogenesis within TME [31, 32]. For instance, in gastric cancer, a positive correlation has been identified between lymphatic vessel invasion, lymph node status, and tissue expression of VEGF-C, with VEGF-C mRNA levels in tumor tissue exceeding those in normal mucosa [33, 34]. These independent findings corroborate the findings of our study, suggesting that PAX5 facilitates GAC angiogenesis through VEGF-C modulation, thereby contributing to tumor progression.

The PI3K/AKT1 signaling pathway is a central pathway in numerous cancers, regulating cell survival, metastasis, and metabolism [35, 36]. For example, activation of this pathway promotes proliferation and migration of glioma and gastric cancer cells [37, 38]. Dysregulation of the PI3K/AKT1 pathway can result from various mechanisms, including mutations in genes such as *PIK3CA*, *PTEN*, *AKT*, *TSC1*, and mTOR [39]. Our findings demonstrate that PAX5 significantly upregulates the expression of both PIK3 and AKT genes and proteins, thereby activating the PI3K/AKT1 pathway and consequently promoting proliferation and invasion of GAC cells. This suggests that PAX5's modulation of the PI3K/AKT1 pathway is a crucial mechanism underlying its pro-tumorigenic effects. Within TME, increased angiogenesis provides tumor cells with enhanced access to nutrients and oxygen, thereby fueling tumor progression. The PI3K/AKT1 signaling pathway also plays a role in angiogenesis and the recruitment of inflammatory mediators. Evidence suggests that the PI3K/Akt pathway promotes TNF-induced endothelial cell migration and regulates tumor angiogenesis; matrix metalloproteinases (MMPs) and cyclooxygenase 2 (COX-2) similarly influence tumor vascularization [40]. Furthermore, VEGF activates the PI3K/Akt pathway through the formation of a VEGF/VEGFR-2 dimer, thus mediating both tumor metastasis and angiogenesis [41]. In breast cancer, the PI3K/Akt signaling pathway mediates IGF-1-induced VEGF-C upregulation, leading to lymphatic metastasis [42]. Our subsequent in vitro co-culture assays further demonstrated that PAX5 overexpression upregulates the expression of VEGF-C and the PI3K/AKT1 signaling pathway, enhancing HLEC cell tube formation. This indicates that the PI3K/AKT1 signaling pathway participates in PAX5-induced VEGFR-C upregulation during GAC lymphatic metastasis, ultimately contributing to metastatic progression.

Finally, we developed a subcutaneous tumor-bearing mouse model. The in vivo findings further validated that PAX5 promotes tumor growth, positively regulates itself and the PI3K/AKT1 signaling pathway, and positively modulates the expression of the angiogenesis-related factor VEGF-C. These in vivo results align with the in vitro

cell assay findings, strongly supporting the critical role of PAX5 in GAC lymph node metastasis.

However, the number of proliferative immune cells identified in this study was relatively small, and the reliability of the obtained results remains to be further verified. Due to the potential randomness and bias that may exist in small-sample cell populations, the applicability and robustness of the derived gene signatures in different samples or cohorts cannot be fully guaranteed, which is an unavoidable research limitation of this study. Notably, the original study of the GSE234129 dataset obtained a much larger scale of cell samples by integrating five single-cell RNA sequencing datasets, which provides sufficient support for the single-cell level analysis of proliferative immune cells. In light of the constructive suggestions from the reviewers, to further improve the robustness of the relevant analyses in this study, more public datasets will be incorporated in our subsequent research to further improve the verification of the gene signatures of proliferative immune cells. Meanwhile, special focus will be placed on combining spatial transcriptome data to deepen the correlation analysis between the spatial distribution and function of proliferative immune cells, thereby further enhancing the scientificity and rigor of the research conclusions.

Conclusion

In this study, combined scRNA-seq and ST technologies were employed to systematically analyze the lymph node metastatic microenvironment of GAC. Eight cell types and six distinct proliferative subpopulations were identified. The functional dynamic characteristics of proliferative B cells transitioning from anti-tumor immunity to an immune escape phenotype were unveiled, and PAX5 was screened as a key gene. A series of experiments confirmed that PAX5 could promote the proliferation, migration, invasion and angiogenesis of GAC cells. Its mechanism of action is closely associated with the regulation of VEGF-C and PI3K/AKT1 signaling pathways. In the future, further exploration of the regulatory network of PAX5 will be conducted. Its potential as a diagnostic marker or prognostic indicator will be evaluated, aiming to provide more effective therapeutic strategies for GAC.

Supplementary Information

The online version contains supplementary material available at https://doi.org/10.1186/s12967-026-08059-4.

Supplementary Material 1

Supplementary Material 2

Supplementary Material 3

Supplementary Material 4

Supplementary Material 5

Supplementary Material 6

Acknowledgements
Not applicable.

Author contributions
Conceptualization: Feng Sun, Chen Liao, Shi Chen, Feng Wang; methodology: Shi Chen, Feng Wang, Li-Xing Wang; formal analysis: Shi Chen, Feng Wang, Yun Gong, Yi-Jun Li; investigation: Shi Chen, Feng Wang, Qing-Wen Xu, Lin-Xing He; data curation: Yu-Xing Qi, Shu-Min Li, Hang Xiong; visualization: Feng Sun, Li-Xing Wang; writing—original draft preparation: Shi Chen, Li-Xing Wang; writing—review and editing: Feng Sun, Chen Liao, Li-Xing Wang, Feng Wang.

Funding
This study was supported by the following projects: the Famous Doctor Project of the Xingdian Talent Support Program of Yunnan Province (Project Title: Prospective Study on Early Diagnosis and Precision Treatment of Gastric Cancer; Project No.: XDYC-MY-2022-0042), the Key Joint Special Project for Basic Research of Kunming Medical University (Project Title: Mechanism Study on TAL2 Promoting Gastric Cancer Progression by Enhancing Aerobic Glycolysis through Regulating TRIB3; Project No.: 202501AY070001-030), and the Science and Technology Talent and Platform Program of Yunnan Province (Project Title: Wang Bin Expert Workstation of Yunnan Province; Project No.: 202205AF150011). The recipient of these projects is Sun Feng.

Data availability
The dataset(s) supporting the conclusions of this article is(are) included within the article (and its additional file(s)).

Declarations

Ethics approval and consent to participate
This study has obtained approval from the Experimental Animal Welfare and Ethics Committee of the Second Affiliated Hospital of Kunming Medical University (Approval No.: kyfey2025041) and the Medical Ethics Committee of the Second Affiliated Hospital of Kunming Medical University (Review Date: August 22, 2022; Approval Date: August 30, 2022; Approval No.: Shen-PJ-Ke-2022-159). All experimental procedures in this study were conducted in accordance with the principles of the Declaration of Helsinki. Written informed consent was obtained from all participants prior to sample collection.

Consent for publication
All authors have given consent to publish.

Competing interests
The authors declare that they have no competing interests.

Author details
[1]Department of Gastrointestinal Surgery, The Second Affiliated Hospital of Kunming Medical University, No. 374, Dianmian Avenue, Wuhua District, Kun Ming, Yun Nan, Yunnan Province 650101, China

Received: 26 September 2025 / Accepted: 18 March 2026
Published online: 16 April 2026

References

1. HAN S, ZHU W, YANG W, et al. A Prognostic Signature Constructed by CTHRC1 and LRFN4 in Stomach Adenocarcinoma[J]. Front Genet. 2021;12:646818. https://doi.org/10.3389/fgene.2021.646818.
2. WANG R, SONG S, QIN J, et al. Evolution of immune and stromal cell states and ecotypes during gastric adenocarcinoma progression[J]. Cancer Cell. 2023;41(8):1407–e14261409. https://doi.org/10.1016/j.ccell.2023.06.005.
3. SUNG H, FERLAY J, SIEGEL RL, et al. Global Cancer Statistics 2020: GLOBOCAN Estimates of Incidence and Mortality Worldwide for 36 Cancers in 185 Countries[J]. CA Cancer J Clin. 2021;71(3):209–49. https://doi.org/10.3322/caac.21660.

4. JIANG H, YU D, YANG P, et al. Revealing the transcriptional heterogeneity of organ-specific metastasis in human gastric cancer using single-cell RNA Sequencing[J]. Clin Transl Med. 2022;12(2):e730. https://doi.org/10.1002/ctm2.730.
5. CHANG J, WU H, WU J, et al. Constructing a novel mitochondrial-related gene signature for evaluating the tumor immune microenvironment and predicting survival in stomach adenocarcinoma[J]. J Transl Med. 2023;21(1):191. https://doi.org/10.1186/s12967-023-04033-6.
6. LIU Y, HE M, TANG H, et al. Single-cell and spatial transcriptomics reveal metastasis mechanism and microenvironment remodeling of lymph node in osteosarcoma[J]. BMC Med. 2024;22(1):200. https://doi.org/10.1186/s12916-024-03319-w.
7. SHIELDS JD, BORSETTI M, RIGBY H, et al. Lymphatic density and metastatic spread in human malignant melanoma[J]. Br J Cancer. 2004;90(3):693–700. https://doi.org/10.1038/sj.bjc.6601571.
8. HIRAKAWA S, BROWN LF. VEGF-C-induced lymphangiogenesis in sentinel lymph nodes promotes tumor metastasis to distant sites[J]. Blood. 2007;109(3):1010–7. https://doi.org/10.1182/blood-2006-05-021758.
9. HIRAKAWA S, KODAMA S, KUNSTFELD R, et al. VEGF-A induces tumor and sentinel lymph node lymphangiogenesis and promotes lymphatic metastasis[J]. J Exp Med. 2005;201(7):1089–99. https://doi.org/10.1084/jem.20041896.
10. HIRZ T, MEI S, SARKAR H, et al. Dissecting the immune suppressive human prostate tumor microenvironment via integrated single-cell and spatial transcriptomic analyses[J]. Nat Commun. 2023;14(1):663. https://doi.org/10.1038/s41467-023-36325-2.
11. ZAVROS Y, MERCHANT JL. The immune microenvironment in gastric adenocarcinoma[J]. Nat Rev Gastroenterol Hepatol. 2022;19(7):451–67. https://doi.org/10.1038/s41575-022-00591-0.
12. RODRIQUES SG, STICKELS RR. Slide-seq: A scalable technology for measuring genome-wide expression at high spatial resolution[J]. Science. 2019;363(6434):1463–7. https://doi.org/10.1126/science.aaw1219.
13. ZHANG L, CHEN D, SONG D, et al. Clinical and translational values of spatial transcriptomics[J]. Signal Transduct Target Ther. 2022;7(1):111. https://doi.org/10.1038/s41392-022-00960-w.
14. LU H, XU Z. High infiltration of immune cells with lower immune activity mediated the heterogeneity of gastric adenocarcinoma and promoted metastasis[J]. Heliyon. 2024;10(17):e37092. https://doi.org/10.1016/j.heliyon.2024.e37092.
15. QIAN Y, ZHAI E, CHEN S, et al. Single-cell RNA-seq dissecting heterogeneity of tumor cells and comprehensive dynamics in tumor microenvironment during lymph nodes metastasis in gastric cancer[J]. Int J Cancer. 2022;151(8):1367–81. https://doi.org/10.1002/ijc.34172.
16. MA L, LUAN Y. Analyze the Diversity and Function of Immune Cells in the Tumor Microenvironment From the Perspective of Single-Cell RNA Sequencing[J]. Cancer Med. 2025;14(5):e70622. https://doi.org/10.1002/cam4.70622.
17. LI Z, LIU S, GAO Z, et al. Dynamic Proteomic Changes in Tumor and Immune Organs Reveal Systemic Immune Response to Tumor Development[J]. Mol Cell Proteom. 2024;23(5):100756. https://doi.org/10.1016/j.mcpro.2024.100756.
18. LAUSS M, DONIA M, SVANE IM, et al. B Cells and Tertiary Lymphoid Structures: Friends or Foes in Cancer Immunotherapy?[J]. Clin Cancer Res. 2022;28(9):1751–8. https://doi.org/10.1158/1078-0432.Ccr-21-1130.
19. GERMAIN C, GNJATIC S, TAMZALIT F, et al. Presence of B cells in tertiary lymphoid structures is associated with a protective immunity in patients with lung cancer[J]. Am J Respir Crit Care Med. 2014;189(7):832–44. https://doi.org/10.1164/rccm.201309-1611OC.
20. WU X, HUANG Q, CHEN X, et al. B cells and tertiary lymphoid structures in tumors: immunity cycle, clinical impact, and therapeutic applications[J]. Theranostics. 2025;15(2):605–31. https://doi.org/10.7150/thno.105423.
21. YANG H, CHEN K, MENG Y, et al. Review: radiotherapy-mediated B cells within the TLS influence the tumor microenvironment[J]. J Immunother Cancer. 2025;13(7). https://doi.org/10.1136/jitc-2025-011617.
22. WANG R, LAN C, BENLAGHA K, et al. The interaction of innate immune and adaptive immune system[J]. MedComm (2020). 2024; 5(10): e714. https://doi.org/10.1002/mco2.714
23. CHANDNANI N, GUPTA I, MANDAL A, et al. Participation of B cell in immunotherapy of cancer[J]. Pathol - Res Pract. 2024;255:155169. https://doi.org/10.1016/j.prp.2024.155169.
24. SARVARIA A, MADRIGAL JA. B cell regulation in cancer and anti-tumor immunity[J]. Cell Mol Immunol. 2017;14(8):662–74. https://doi.org/10.1038/cmi.2017.35.
25. MONTESINOS-RONGEN M, VAN ROOST D, SCHALLER C, et al. Primary diffuse large B-cell lymphomas of the central nervous system are targeted by aberrant somatic hypermutation[J]. Blood. 2004;103(5):1869–75. https://doi.org/10.1182/blood-2003-05-1465.
26. WANG T, CHEN Z, LI C, et al. PAX5 and circ1857 affected DLBCL progression and B-cell proliferation through regulating GINS1[J]. Cancer Sci. 2023;114(8):3203–15. https://doi.org/10.1111/cas.15856.
27. LIU SL, CAI C, YANG ZY, et al. DGCR5 is activated by PAX5 and promotes pancreatic cancer via targeting miR-3163/TOP2A and activating Wnt/β-catenin pathway[J]. Int J Biol Sci. 2021;17(2):498–513. https://doi.org/10.7150/ijbs.55636.
28. O'BRIEN P, OUELLETTE MORINPJR. The Pax-5 gene: a pluripotent regulator of B-cell differentiation and cancer disease[J]. Cancer Res. 2011;71(24):7345–50. https://doi.org/10.1158/0008-5472.Can-11-1874.
29. NASRI NASRABADI P MARTIND. The Pleiotropy of PAX5 Gene Products and Function[J]. Int J Mol Sci. 2022;23(17). https://doi.org/10.3390/ijms231710095.
30. FERRARA N, GERBER HP, LECOUTER J. The biology of VEGF and its receptors[J]. Nat Med. 2003;9(6):669–76. https://doi.org/10.1038/nm0603-669.
31. DUFF SE, LI C, JEZIORSKA M, et al. Vascular endothelial growth factors C and D and lymphangiogenesis in gastrointestinal tract malignancy[J]. Br J Cancer. 2003;89(3):426–30. https://doi.org/10.1038/sj.bjc.6601145.
32. KONG D, ZHOU H. VEGF-C mediates tumor growth and metastasis through promoting EMT-epithelial breast cancer cell crosstalk[J]. Oncogene. 2021;40(5):964–79. https://doi.org/10.1038/s41388-020-01539-x.
33. ICHIKURA T, TOMIMATSU S. Prognostic significance of the expression of vascular endothelial growth factor (VEGF) and VEGF-C in gastric carcinoma[J]. J Surg Oncol. 2001;78(2):132–7. https://doi.org/10.1002/jso.1133.
34. YONEMURA Y, ENDO Y, FUJITA H, et al. Role of vascular endothelial growth factor C expression in the development of lymph node metastasis in gastric cancer[J]. Clin Cancer Res. 1999;5(7):1823–9.
35. LAWRENCE MS, STOJANOV P, MERMEL CH, et al. Discovery and saturation analysis of cancer genes across 21 tumour types[J]. Nature. 2014;505(7484):495–501. https://doi.org/10.1038/nature12912.
36. HE Y, SUN MM, ZHANG GG, et al. Targeting PI3K/Akt signal transduction for cancer therapy[J]. Signal Transduct Target Therapy. 2021;6(1):425. https://doi.org/10.1038/s41392-021-00828-5.
37. WANG B, ZHAO CH. IL-17 induces the proliferation and migration of glioma cells through the activation of PI3K/Akt1/NF-κB-p65[J]. Cancer Lett. 2019;447:93–104. https://doi.org/10.1016/j.canlet.2019.01.008.
38. AKRAMI H, MAHMOODI F, HAVASI S, et al. PlGF knockdown inhibited tumor survival and migration in gastric cancer cell via PI3K/Akt and p38MAPK pathways[J]. Cell Biochem Funct. 2016;34(3):173–80. https://doi.org/10.1002/cbf.3176.
39. SLOMOVITZ BM, COLEMAN RL. The PI3K/AKT/mTOR pathway as a therapeutic target in endometrial cancer[J]. Clin Cancer Res. 2012;18(21):5856–64. https://doi.org/10.1158/1078-0432.Ccr-12-0662.
40. ZHANG R, XU Y, EKMAN N, et al. Etk/Bmx transactivates vascular endothelial growth factor 2 and recruits phosphatidylinositol 3-kinase to mediate the tumor necrosis factor-induced angiogenic pathway[J]. J Biol Chem. 2003;278(51):51267–76. https://doi.org/10.1074/jbc.M310678200.
41. BYRNE AM, BOUCHIER-HAYES DJ HARMEYJH. Angiogenic and cell survival functions of vascular endothelial growth factor (VEGF)[J]. J Cell Mol Med. 2005;9(4):777–94. https://doi.org/10.1111/j.1582-4934.2005.tb00379.x.
42. ZHU C, QI X, CHEN Y, et al. PI3K/Akt and MAPK/ERK1/2 signaling pathways are involved in IGF-1-induced VEGF-C upregulation in breast cancer[J]. J Cancer Res Clin Oncol. 2011;137(11):1587–94. https://doi.org/10.1007/s00432-011-1049-2.

Publisher's note